Some Practical Applications of CFD Analysis to Aerodynamic Design Of the Supersonic Experimental Airplane

Naoki Futatsudera (Mitsubishi Heavy Industries, Ltd., naoki_futatsudera@mx.nasw.mhi.co.jp)

Takeshi Kaiden (Mitsubishi Heavy Industries, Ltd., takeshi_kaiden@mx.nasw.mhi.co.jp)

Abstract

In 1997, National Aerospace Laboratory (NAL) started a program to develop a scaled supersonic experimental airplane to establish the technological basis for the development of the next generation supersonic transport. A non-powered experimental airplane is being developed for the first experimental flight in 2002. The airplane is launched by a rocket-booster. After the rocket-booster is separated, the airplane starts the measurement flight at Mach 2.0 and altitude 18.5km.

In the aerodynamic design of the experimental airplane, Mitsubishi Heavy Industries, Ltd. (MHI) is in charge of the overall design and NAL mainly conducted the wing and wing-body aerodynamic integration design with their sophisticated CFD code. MHI is also in charge of the launch configuration aerodynamic design.

In the MHI design work, wind tunnel test data were mainly used. Some experimental data were checked and corrected using the CFD analysis.

CFD analysis also played an important role in understanding physical phenomena of the complicated flow field of the experimental airplane and the rocket-booster.

1. Introduction

In 1997, NAL started the program called NEXST (National Experimental Supersonic Transport) to establish the technological basis for the development of the next generation supersonic transport [1]. Two types of unmanned airplanes, i.e., a non-powered and a jet-powered airplane, will be built.

A non-powered experimental airplane (Fig.1) is being developed for the first experimental flight in 2002. The main purpose of the experimental flight with this airplane is to verify the aerodynamic design methodology with CFD, especially the supersonic natural laminar flow wing design. The airplane is launched by a rocket-booster (Fig.2) to the separation point (altitude 19.5km, Mach number 2.1). After the separation of the rocket-booster, the airplane starts the measurement flight at Mach 2.0 and at altitude 18.5km and descends to altitude 12km maintaining Mach number constant. In the measurement flight, surface pressure distribution and boundary layer transition are measured. After decelerating and descending to the recovery point, the experimental airplane lands on the ground using a parachute and airbags (Fig.3).

In the aerodynamic design of the experimental airplane, MHI is in charge of overall design (wing location and tail sizing, etc.) and NAL mainly conducted the wing and wing-body aerodynamic integration design with their sophisticated CFD code. And MHI is also in charge of the design of the launch configuration (airplane connected to the rocket-booster).

This paper describes the role of CFD analysis and four practical applications in our aerodynamic design work.

2. CFD Analysis in the Aerodynamic Design

In this MHI aerodynamic design, we used several aerodynamic analysis methods according to the design phase.

In the basic design phase, design handbook and the linear aerodynamic theory were mainly used for the design of an initial configuration and its modification. They do not take much time and are very easy to use. They also have enough

accuracy in this design phase.

And the basic wind tunnel tests were conducted for verification.

CFD analysis was mainly used to understand the physical phenomena of the complicated flow field. Some CFD analyses were also conducted for estimation of aerodynamic difference caused by configuration change, and also for complement of the wind tunnel test results. CFD analysis was used mainly for the launch configuration design. Aerodynamic coefficients of launch configuration include much interference effect and which is difficult to estimate by the other simpler methods.

In the detail design phase, the aerodynamic configuration was almost fixed. The detail wind tunnel tests were conducted and final aerodynamic data were developed based on that complete wind tunnel test data. So CFD analysis was mainly used in understanding the local physical phenomena and checking and correcting the experimental data.

In the design work, design tools are always chosen based on the trade-off between accuracy and time and cost for efficiency in design work. Applications of CFD analysis were restricted in our design work because of the following reasons:

- Taking time for modeling and calculation
- Less accurate in detail design
- Difficult in the detail modeling
- Not easy to use (Specialists are needed)

3. CFD Method

CFD method used in following examples is as follows.

(Grid Generation)

Chimera technique [2]-[3] is applied to this computation. The grids used in this method are generated independently for the each component, i.e., the experimental airplane (wing / fuselage / vertical tail), horizontal tail, rocket-booster. The number of the grids for half model used here is shown in the Tab.1. These grids are generated by the algebraic interpolation method.

The differences between CFD model and wind tunnel model are as follows. First, CFD model does not simulate many protuberances (antennas, connection parts between the experimental airplane and the rocket-booster etc. shown in Fig.1 and Fig.2). Secondly, space-gaps between the rocket-booster fin and the deflected control surface are not simulated.

The grid for the isolated airplane computation is shown in Fig.4. The grid of the horizontal tail is overset in this computation. Fig.5 shows the grid for computation of the launch configuration and configuration in the separation procedure. In these configurations, the grid of the rocket-booster is overset.

(Flow Solver)

The governing equations are three-dimensional thin layer Reynolds-averaged Navier-Stokes equations. The convective term is discretized using Roe's flux difference splitting with MUSCL [4]. LU-ADI implicit method is adopted in time integration. The local time stepping is used to accelerate the convergence of the iteration. The turbulence model used here is an algebraic model of Baldwin-Lomax type.

The solution process of Chimera technique is described in Fig.6. First, physical properties of the hole on the mother grid are interpolated from those of the child grid (Process A). The hole stated here is defined as the location where the flow properties are set from those of the other grids. After the interpolation, the flow computation on the mother grid is performed (Process B). At this time, flow computation is not performed on the hole of mother side. At the next step, physical properties of the hole on the child grid are interpolated from those of the mother grid (Process C). Finally, the flow computation on the child grid is done (Process D). The hole is treated in the same manner of the mother computation. This process is repeated until the residual is less than the designated value.

4. Practical Applications of CFD Analysis

The following four examples show the important role of the CFD analysis in our design work.

4.1 Stabilizer Hinge-moment

The basic wind tunnel test was conducted for the 3rd experimental airplane configuration and the detail wind tunnel test was conducted for the 4th experimental airplane configuration. The stabilizer hinge-moments measured by both wind tunnel tests were far different from each other against the prediction (Fig.7).

By the review of the experimental data, it was

found that difference partly resulted from the measurement errors and which were corrected with the CFD results.

The stabilizer hinge-moment was measured by the one-component internal (hinge-moment) balance. It would be under the interference of stabilizer lift and bending moment to some extent (Fig. 8). That means some lift force and bending moment are measured as hinge-moment. By detailed balance calibration of internal balances of 3rd and 4th configuration wind tunnel model, the interference factors were measured.

Both wind tunnel hinge-moment data were corrected with these interference factors and stabilizer lift and bending moment calculated by CFD. Filled symbols in Fig.7 represent the corrected data. Corrected data of 3rd and 4th configuration are almost same each other in supersonic region.

Corrected data seemed more reasonable, but the latter wind tunnel test data (○) are used as the design nominal considering more aerodynamic design margin.

This hinge-moment increment reduced the design margin of an actuator performance, but margin is still enough.

4.2 Rocket-booster Control Surface Hinge-moment

Launch configuration controls maneuvers with conventional rudder type control surfaces at four rocket fins.

The basic wind tunnel test was conducted for the 1st launch configuration and the detail wind tunnel test was conducted for the 3rd launch configuration. The fin control surface hinge-moments data measured by both wind tunnel tests were far different from each other at transonic speed (Fig.9). Both test data show good agreement under Mach 0.9 and over Mach 1.6, and no measurement failures were found at every test Mach numbers. So it had been supposed that difference would be caused by an aerodynamic phenomenon.

By review with the CFD analysis, it was found that configuration difference of the rocket-booster body-end of both launch configurations was the trigger of the hinge-moment difference (Fig.10). The 1st launch configuration wind tunnel model had the gimbal base. De-touched shock from gimbal base was supposed to make difference of fin control surface hinge-moment at the transonic speed (Fig.11).

CFD calculations of both launch configurations were conducted at three Mach numbers. Fig.12 shows comparison of the surface pressure distributions of the rocket-booster aft-body of both 1st and 3rd launch.

It shows that flow fields near the fin control surfaces of the former and latter configuration are similar at Mach 0.6 and Mach 2.0, but different at Mach 1.2. The control surfaces are affected by high-pressure region caused by the gimbal base. This will be the reason of difference in fin control surfaces hinge-moment.

Fig.13 shows comparison of CFD result with wind tunnel test data of the latter configuration (3rd). The test data and CFD results show good agreement at every Mach numbers. The wind tunnel test data for the 3rd configuration were used as the design nominal for the final launch configuration.

4.3 Launch Configuration Cm_0 at Mach 2.0

Wind tunnel test data showed that the 3rd launch configuration has large amount of negative Cm_0 (moment coefficient at zero degree angle of attack) around Mach 2.0 (Fig.14). And it was also shown that the rocket-booster had negative Cm_0 by the component-force measurement of the airplane of the launch configuration in the wind tunnel test.

The control authority would be short so as to keep the launching maneuver profile because of this large negative Cm_0 and small fin control surface effectiveness around Mach 2.0.

CFD calculation was conducted at Mach 2.0, zero degree angle of attack so as to make this phenomenon clear. Fig. 15 shows the ΔCm_0 per unit length of both the experimental airplane and the rocket-booster. This figure shows which part makes negative Cm_0. It is found that the rocket fins mainly make large negative ΔCm_0 of the launch configuration. It is supposed that expansion waves between the fuselage of the experimental airplane and the rocket body affects the aerodynamic characteristics of the rocket fins.

So large negative Cm_0 was understood as reasonable, launching maneuver profile was revised from the initial one.

4.4 Interference Force at the Separation

The safety separation is the final step for the successful measurement flight. But it was predicted that wing and large rocket fins made

large amount of aerodynamic interference force and which resulted in complicated separation maneuver.

Separation flight simulations were conducted so as to establish the requirement for the separation without re-contacts.

The aerodynamic characteristics used in the separation flight simulation were based on the grid wind tunnel test [5] data.

Although wind tunnel test was useful for preparing the large number of aerodynamic characteristic data with enough accuracy, it was often difficult to understand the physical phenomena of the interference force. In these cases, CFD analysis was very helpful.

With CFD results, mechanism of aerodynamic interference force at the separation is analyzed as follows.

Fig.16(1) shows the aerodynamic interference component of pitching moment (Δ Cm) of the experimental airplane (wind tunnel test data).

$\Delta Cm = Cm\_grid - Cm\_isolated$

,where Cm_grid means Cm including the aerodynamic interference, and Cm_isolated means Cm of the isolated airplane.

It is noticed that this graph shows just Δ Cm variation versus Δ Z of the grid wind tunnel test, not of the actual separation maneuver. Δ Z means the normal distance between the experimental airplane and the booster-rocket (Fig.17).

Four projections are found in the Δ Cm variation according to Δ Z. The oblique shock from the rocket-booster nose strikes the airplane, and that results in Δ Cm of the airplane. Fig.18 is the schlieren photographs of same grid wind tunnel test case as that shown in Fig.16. The strike point on the airplane moves backward as Δ Z increases. That makes Δ Cm variation. Four projections successively occur when the oblique shock strikes the fore-body, wing (the front part), wing (the rear part) and horizontal tail of the airplane.

This mechanism of aerodynamic interference can be easily understood with Fig.19. Fig. 19 shows the pressure distribution on the surface and X-Z plane estimated by CFD corresponding to the grid wind tunnel test case shown in Fig.16 and Fig.18. Fig.19 (1) is at $\Delta Z = 1m$, where the oblique shock from the rocket-booster nose is about to strike the wing. And Fig. 19 (2) is at $\Delta Z = 2m$, where the oblique shock strikes the middle of the wing and the large compression region can be found on the wing lower surface.

As mentioned above, the aerodynamic interference on the experimental airplane mainly results from the oblique shock from the rocket-booster nose.

Fig.16(2) shows the aerodynamic interference on pitching moment (Δ Cm) of the rocket-booster (wind tunnel test data).

One peak can be found in the Δ Cm variation according to Δ Z increasing. This variation is simpler than for the experimental airplane, but the mechanism of the interference is more complicated. Δ Cm consists of effect of the experimental airplane and effect of the reflected oblique shock from its own nose. The oblique shock from the rocket-booster nose strikes the airplane, and that is reflected. The reflected shock strikes the rocket-booster.

This mechanism can be easily found in Fig.19. In Fig.19 (1), the oblique shock from the rocket-booster nose strikes the intersection part of wing and fuselage, and the reflected shock strikes the rocket-booster mid-body.

In Fig. 19 (2), oblique shock strikes mid part of the wing, and the reflected shock strikes the rocket-booster aft-body and large fins. The reflected shock can be vaguely observed in the schlieren photograph (Fig.18, center). High-pressured region can be found on the lower fins. When the oblique shock strikes the wing, reflected shock is distinct. And when that distinct shock strikes the rocket-booster fins, large amount of interference on pitch-up moment makes peak in Δ Cm variation (at $\Delta Z=2m$ in Fig.16(2)).

Fig. 16 also shows Δ Cm estimated by CFD compared to wind tunnel test data.

For the interference on the experimental airplane, CFD result shows quite good agreement with wind tunnel test data. But for the rocket-booster, large error can be found at small Δ Z. The rocket-booster has several protuberances on its surface. But CFD model does not have these because of difficulty in the detail modeling as mentioned in the section 3.1. This is supposed to mainly cause the error.

CFD analysis could be used to estimate aerodynamic interference on the airplane but not the rocket-booster.

5. Conclusion

Four practical applications of CFD analysis to

the aerodynamic design of the experimental airplane and its launch configuration are presented.

Wind tunnel test data were mainly used for the design but the experimental data were checked and corrected by the CFD.

CFD analysis also played an important role in understanding physical phenomena of the complicated flow field of the experimental airplane and the rocket-booster.

Acknowledgments

The authors are very grateful for the assistance, support and efforts of researchers in NAL working for National Experimental Supersonic Transport (NEXST) program.

Reference

1. Sakata, K., "Supersonic Research Program in NAL, Japan," International CFD Workshop on Super-Sonic Transport Design, Tokyo, Mar. 1998.
2. NASA Ames Space Shuttle Flow Simulation Group, Buning, P., Chiu, I., Martin, F., Meakin, R., Obayashi, S., Rizk, Y., Steger, J., and Yarrow, M., "Numerical Simulation of the Integrated Space Shuttle Vehicle in Ascent," 4th internat. Conf. on Super Computing, Santa Clara, Calif., Apr. 1989.
3. Kaiden, T., Shibata, M. and Iwamiya, T., "Numerical Simulation with Bleed and Bypass Effects of Nacelles on SST," International CFD Workshop for Super-Sonic Transport Design, NAL, March, 1998
4. Fujii, K. and Obayashi, S., "High-Resolution Upwind Scheme for Vortical Flow Simulations," J. Aircraft, Vol.26, No.12, Dec., 1989 pp.1123-1130.
5. Ohyama, K., Kaiden, T., Futatsudera, N. and Shimbo, Y., "Rocket-Booster Separation Wind Tunnel Test of Scaled Supersonic Experimental Airplane," 37th Aircraft Symposium, Tokyo, Oct. 1999.

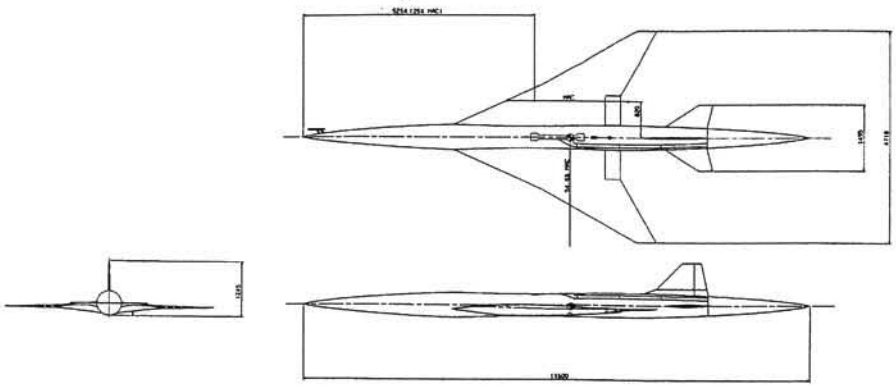

Fig.1 Non-powered experimental airplane

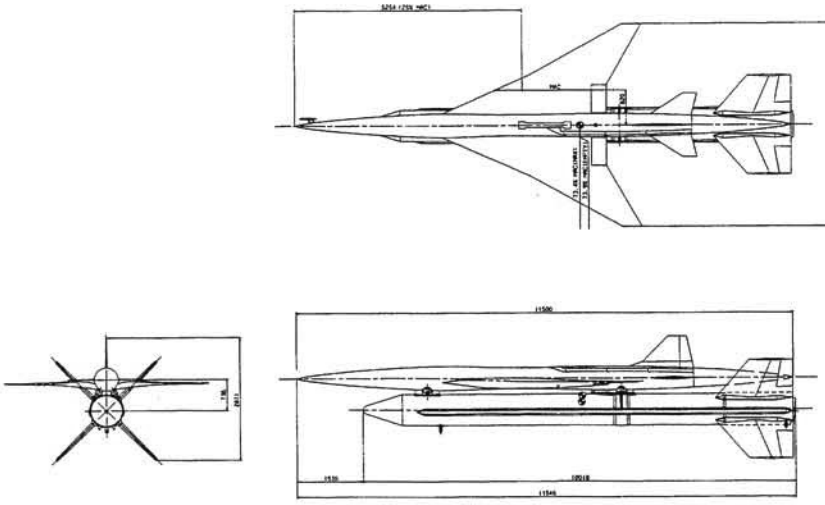

Fig.2 Launch configuration
(combination of experimental airplane and rocket-booster)

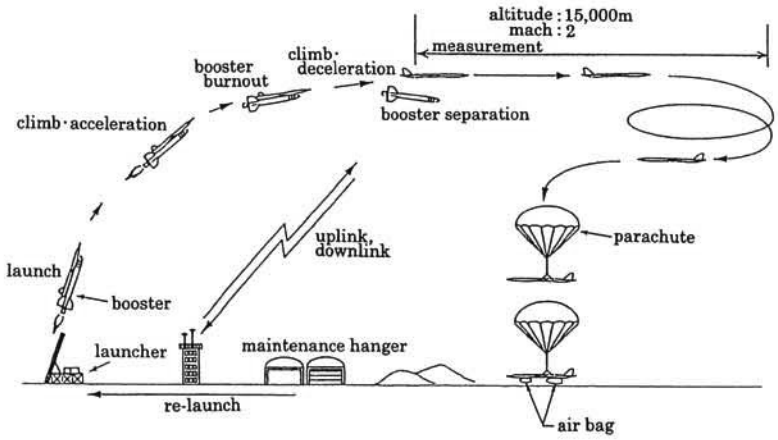

Fig.3 Experimental flight profile

Table.1 The number of the grids

	Experimental Airplane (isolated)	Launch Configuration
Experimental Airplane (*) Grid	1,642,200	2,326,450
Horizontal Stabilizer Grid	323,400	
Rocket-booster Grid	–	1,334,550
Total	1,965,600	3,661,000

(*) horizontal stabilizer less configuration

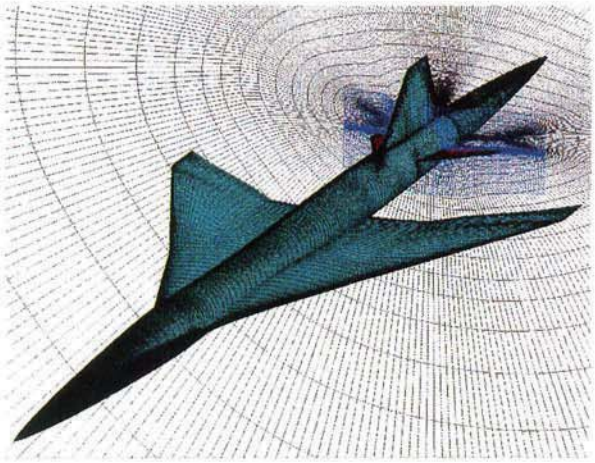

Fig.4 Grid for the computation of the isolated airplane

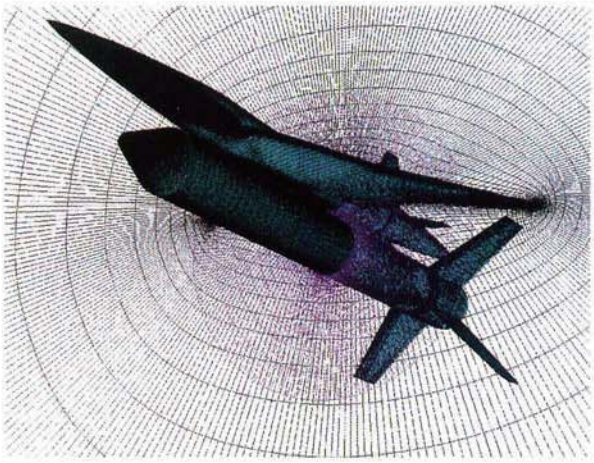

Fig.5 Grid for the computation of the launch configuration

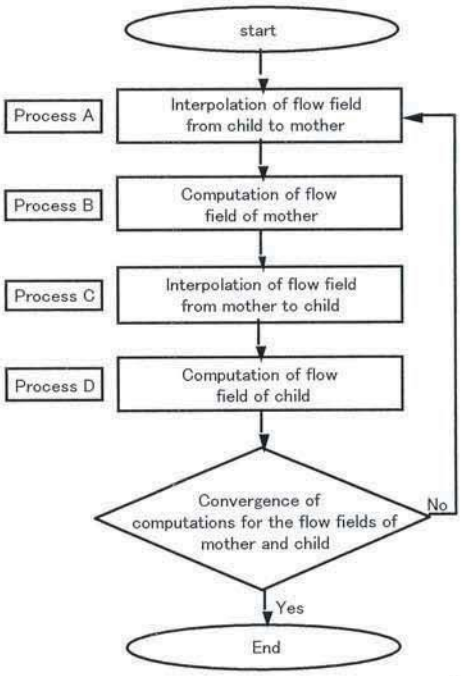

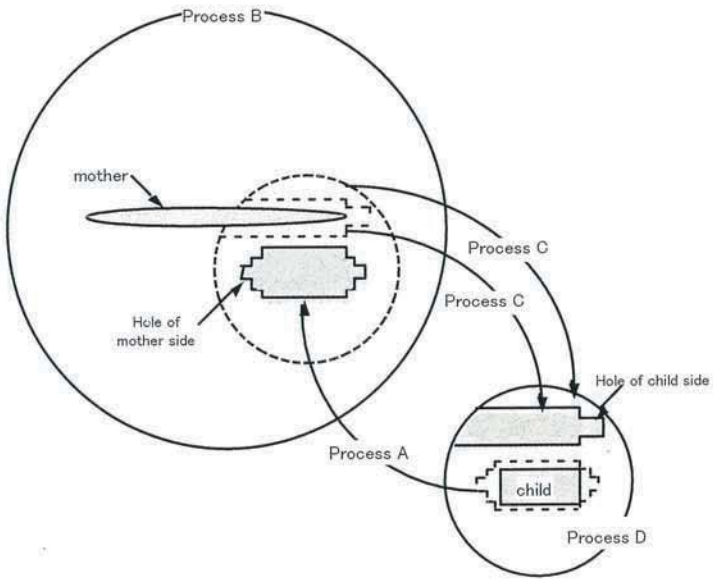

Fig.6 Flow chart of computation

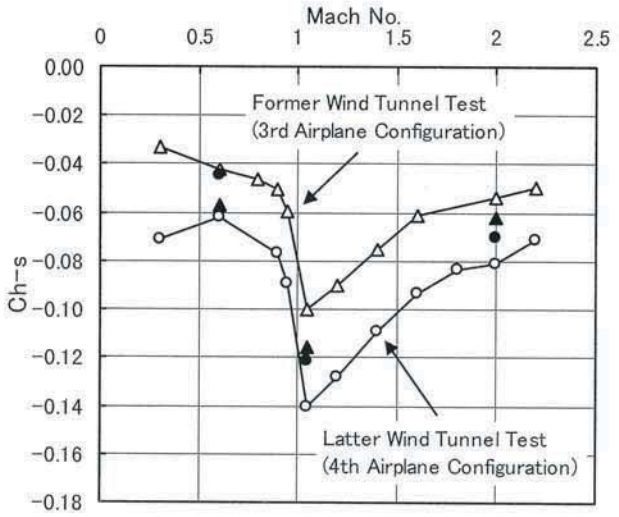

Fig.7 Hinge moment coefficients of horizontal stabilizer (pitch-up 10° , α=0°)

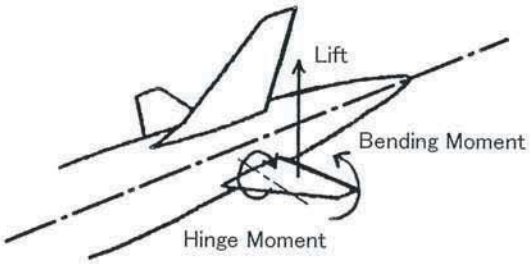

Fig.8 Horizontal stabilizer hinge moment and its interference sources

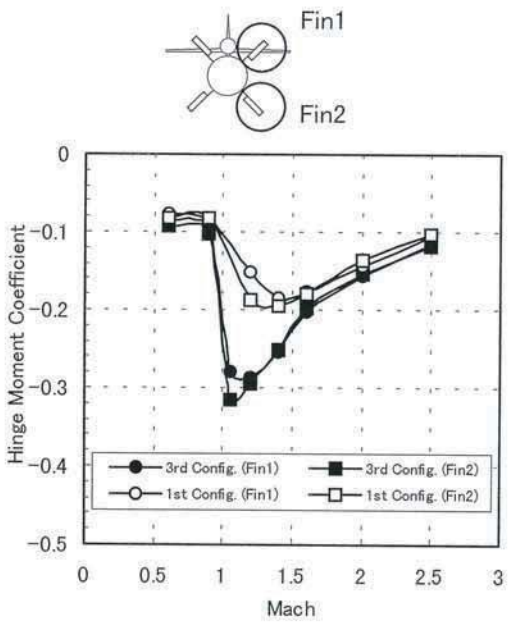

Fig.9 Comparison of hinge moment coefficients (roll10° , α=0°)

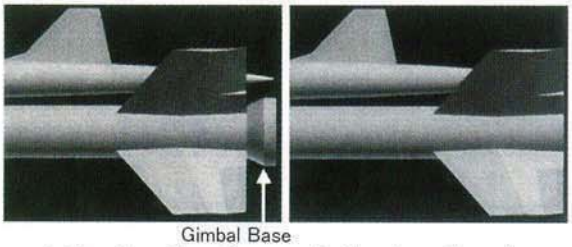

Fig.10 Difference of the rocket-booster aft-body configuration

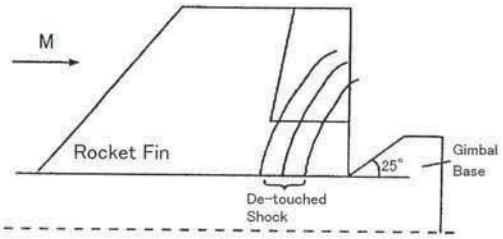

Fig.11 Schema of de-touched shock from the gimbal base at M1.2

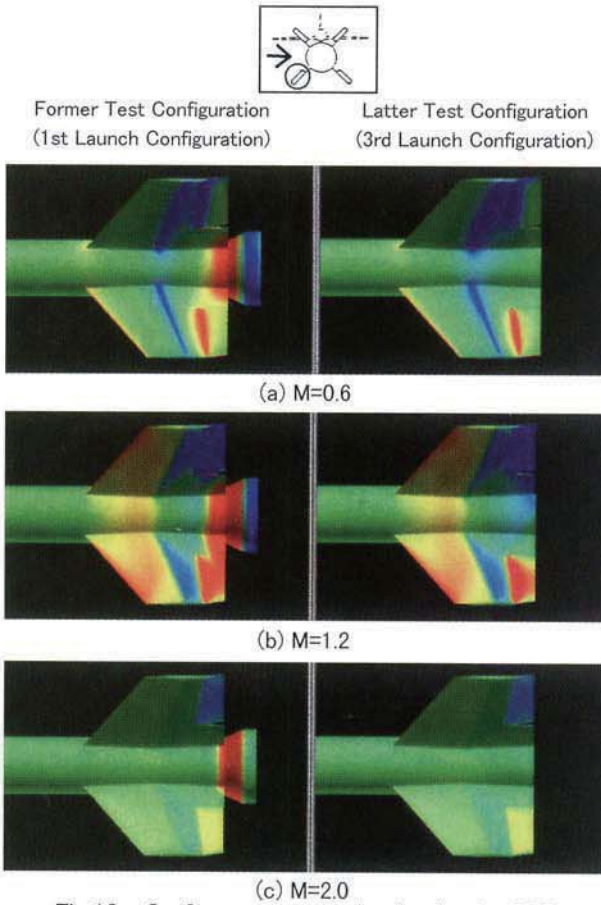

Fig.12 Surface pressure distribution by CFD (The rocket-booster aft-body)

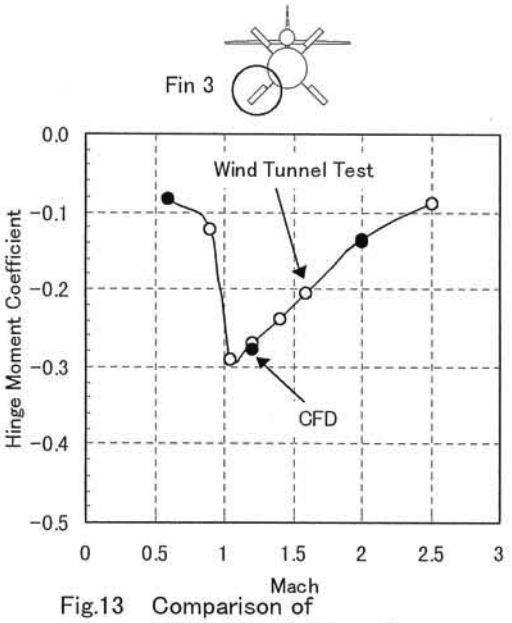

Fig.13 Comparison of CFD with wind tunnel test

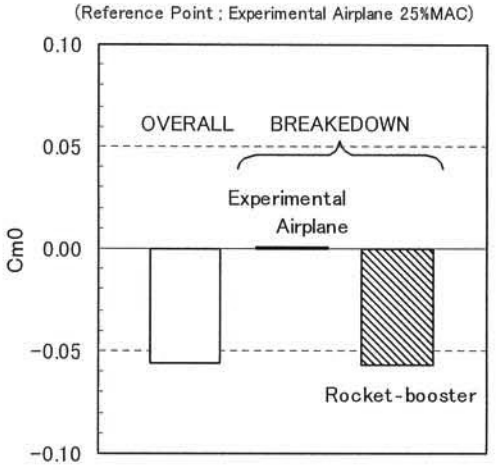

Fig.14 Pitching moment coefficient of launch configuration (M=2.0, α=0°)

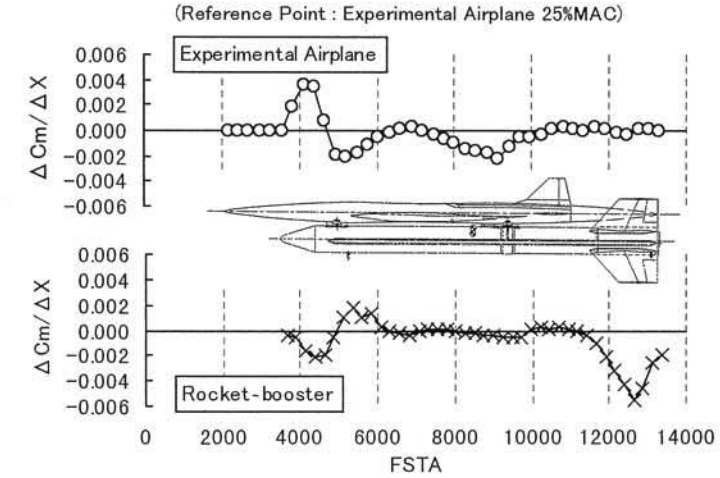

Fig.15 Pitching moment distribution of the launch configuration (M=2.0, α=0°)

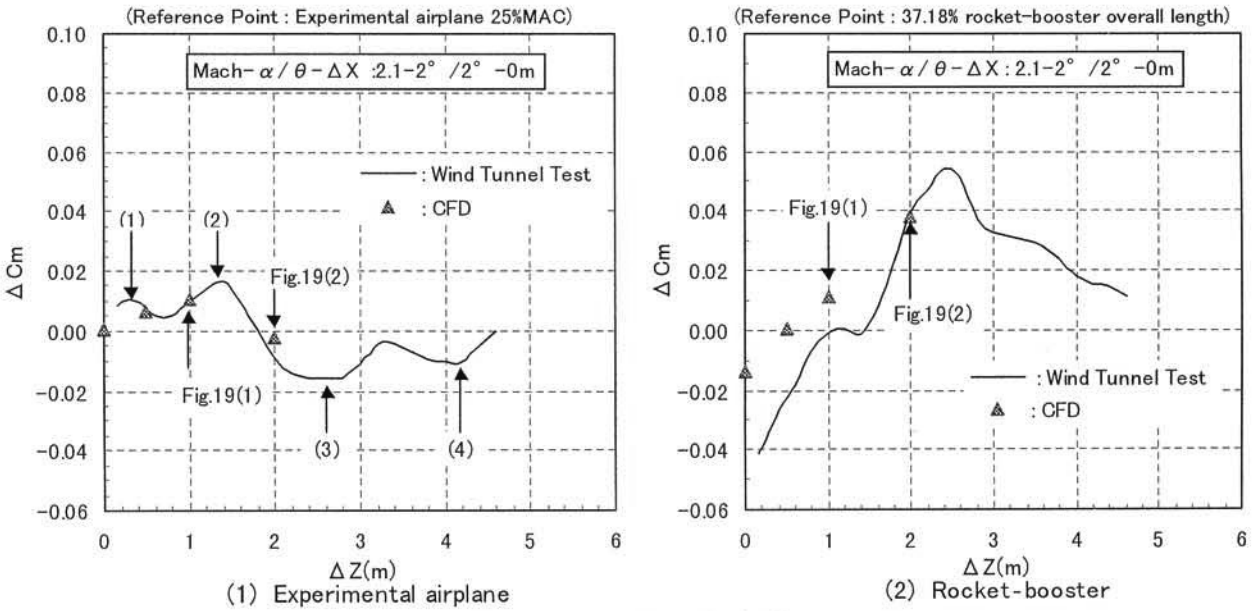

Fig.16 Interference component of pitching moment

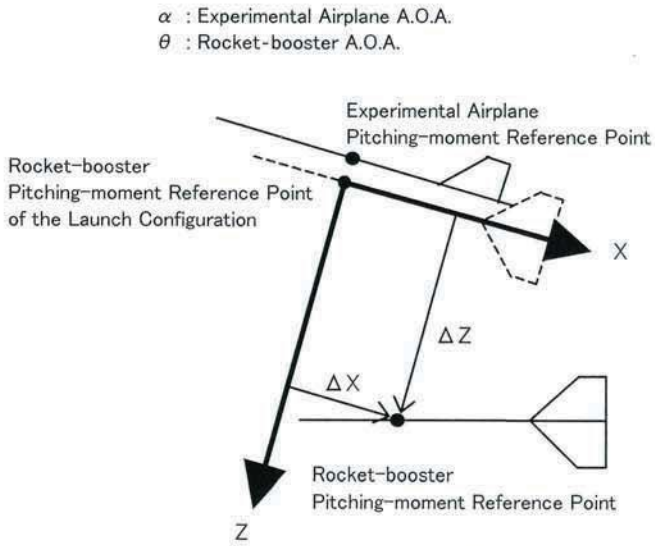

Fig.17 Definition of parameters

(1)～(4) : See Fig.16(1)

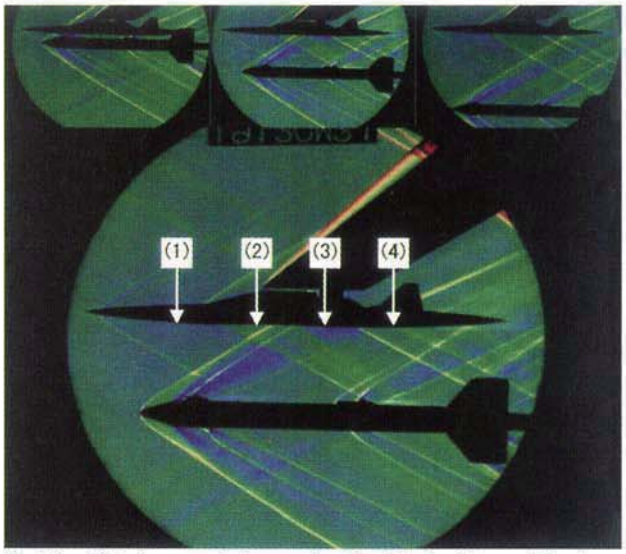

Fig.18 Schlieren photograph of grid wind tunnel test (Mach-α / θ - ΔX : 2.1-2° /2° -0m)

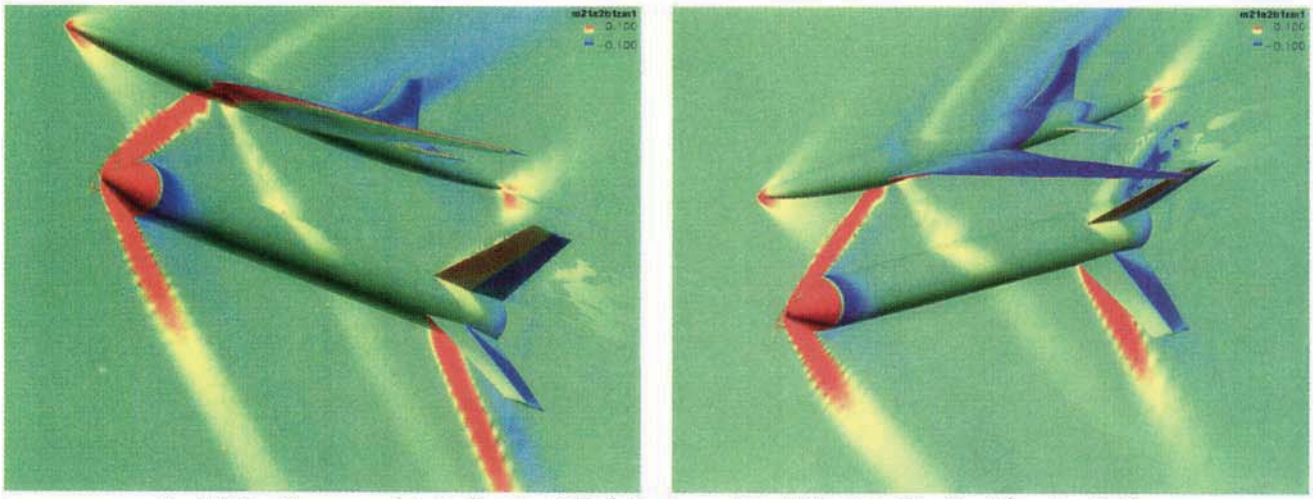

Fig.19(1) Pressure distribution by CFD (Mach-α / θ - ΔX/ ΔZ : 2.1-2° /2° -0m/1m)

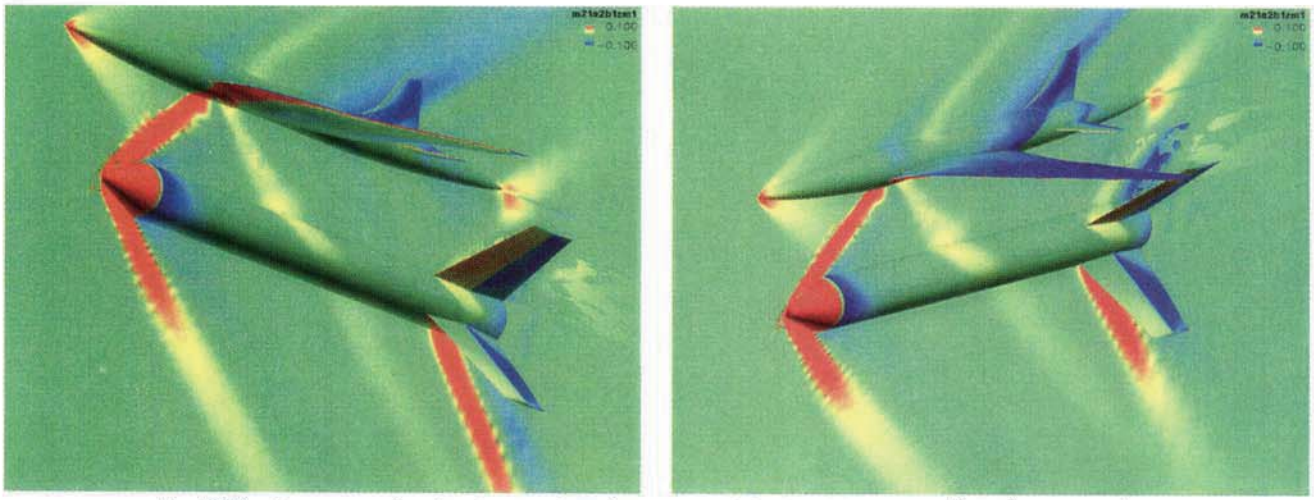

Fig.19(2) Pressure distribution by CFD (Mach-α / θ - ΔX/ ΔZ : 2.1-2° /2° -0m/2m)